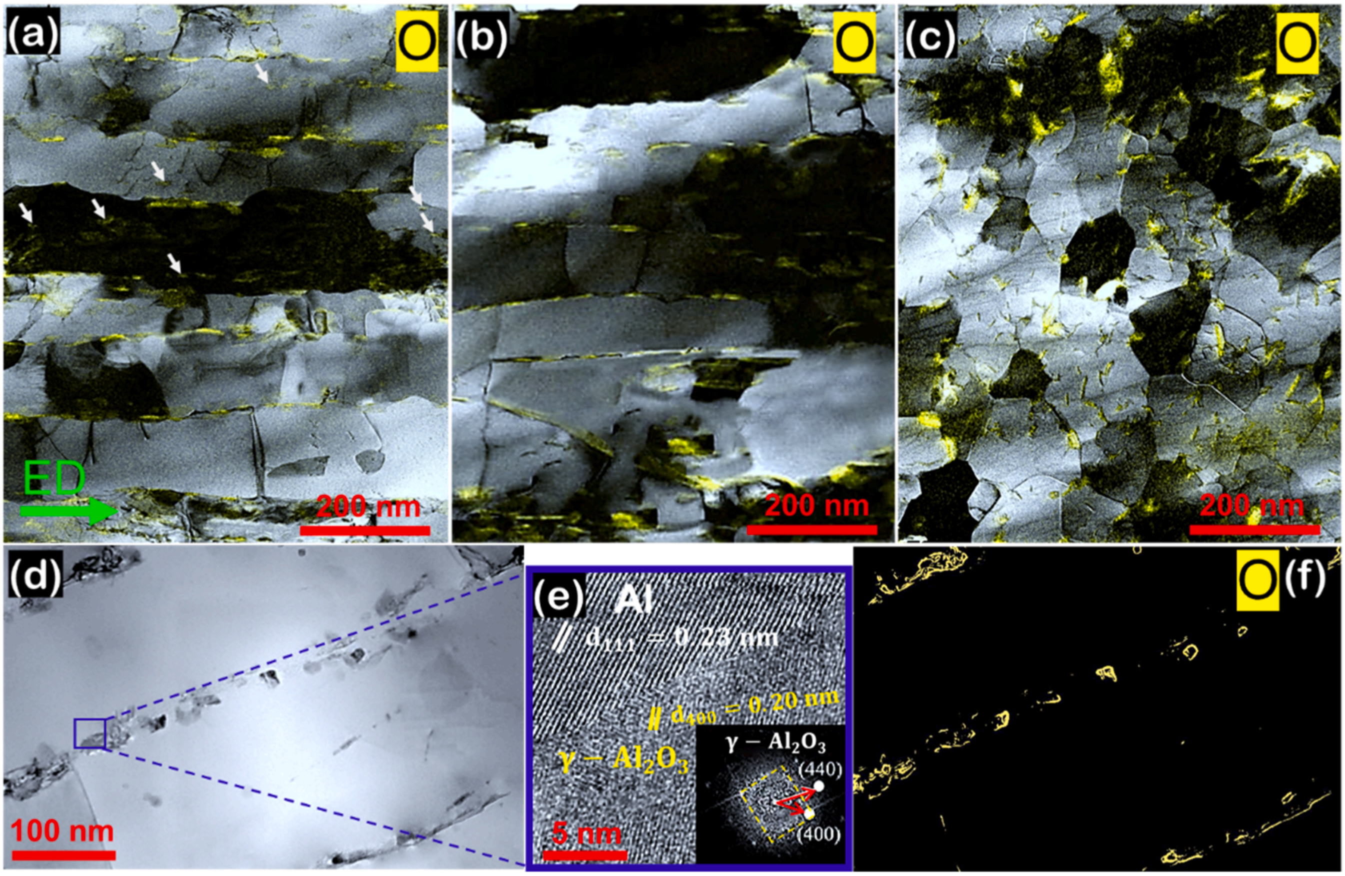

Fig. 7. Combined TEM images and EDS maps of (a) 15 min cold welding, (b) 1 h cold weld and (c) 2 h cold welding; (d-f) STEM images of the 15 min cold welded sample; (d) bright field TEM image, (e) HRTEM showing the structure of γ- Al_2O_3, (f) EDS oxygen map of (d). The white and green arrows show Al_2O_3 nanoplatelets in the grain interior and the ED, respectively. The dash-cube included in Fig. 7(e) demonstrates a cubic lattice structure.

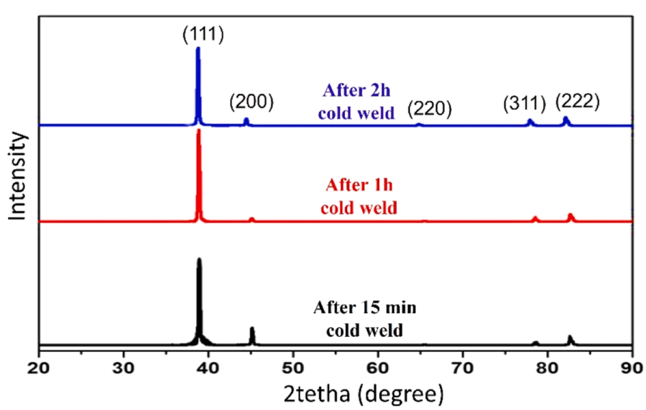

Fig. 8. XRD patterns of the extruded sample with different cold-welding time.

respectively. For 15 min cold weld sample, few Al_2O_3 nanoplatelets are located inside the grains as shown in Fig. 7(a), and, hence, the $\Delta\sigma_{OR}$ can be neglected. According to Jiang's study [55], the in-situ formed Al_2O_3 nanoplatelets between two lamellar grains was 10 nm thick, so the total volume fraction of the Al/Al_2O_3 composites should be 2.8 % ([14/500]× 100) (7 nm thick Al_2O_3 film on the top and bottom of the 500 nm thick Al flake). The Al_2O_3 introduced during cold welding process is assumed to be little, since the Al flakes were well protected under argon atmosphere in the jars. $\Delta\sigma_{GND}^{CTE}$ and $\Delta\sigma_{GND}^{EM}$ can be calculated using the equations in [58,59]. The calculated strengthening contributions are listed in the Table. 2.

The load transfer contributions,$\Delta\sigma_{Al_2O_3}^{L-T}$, is drawn back form the equation:

$$\Delta\sigma_{Al_2O_3}^{L-T} = \sigma_y - \sigma_{ym} = \sigma_y - \left(\sigma_0 + \Delta\sigma_{H-P} + \Delta\sigma_{Al_2O_3}^{dis}\right) \tag{13}$$

The strengthening efficiency R:

$$R = \left(\Delta\sigma_{(Al_2O_3)}^{(L-T)}\right) \Big/ (V_R y_m) \times 100 \tag{14}$$

The data in Table 2 show that the increase in the relative yield strength of the 1 h and 2 h cold weld samples is primarily due to grain refinement. On the other hand, the 15-min cold weld sample shows the highest strength efficiency of Al_2O_3, which is due to the presence of well-aligned Al_2O_3 nanoplatelets along the boundaries of the lamellar structures. This result is consistent with the finding that the alignment of reinforcing elements with a significant aspect ratio can increase their strength efficiency. As the duration of cold-welding increases, the strengthening efficiency of Al_2O_3 gradually decreases, reaching values of 19.83 and 18.68 for the 1 h and 2 h cold welded specimens, respectively. The severe plastic deformation that occurs during cold welding significantly disturbs the arrangement of the Al_2O_3 nanoplatelets, leading to disordered alignment and consequently reducing the strengthening efficiency. The significant lack of differences in the 'strengthening contributions' between the three samples listed in Table 2 can be explained by looking at the individual reinforcement contributions. Indeed, the influence of grain refinement on the strengthening process had the greatest impact and clearly showed how variations in cold welding times affected the grain structure and consequently the mechanical properties. Furthermore, the effectiveness of the Al_2O_3 nanoplatelets in the consolidation process was highlighted

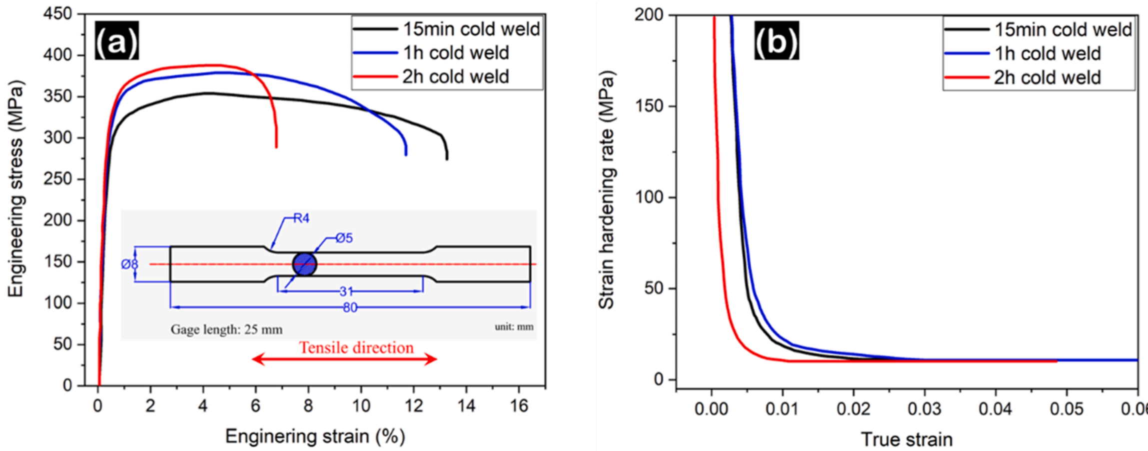

Fig. 9. (a) Tensile stress-strain curves of the samples with different architectures. (b) Strain hardening rate curves of the samples with different architectures.

Table 1
Detailed data of the tensile stress-strain curves.

Cold weld time	Yield Strength $0.2\sigma_{YS}$ (MPa)	Ultimate Strength σ_{UTS} (Mpa)	Total Elongation ε_t (%)	Uniform Elongation ε_u (%)
15 min	283±4	356±11	13.3 ± 0.5	4.3 ± 0.2
1h	302±6	379±9	11.7 ± 0.6	5.1 ± 0.3
2h	315±7	390±14	6.7 ± 0.4	3.3 ± 0.6

by emphasizing their orientation along lamellar structures and explaining how this orientation affected the overall mechanical performance of the composite. In addition to the higher strengthening efficiency, the 15 min cold weld sample with nanolaminate architecture also presents much enhanced ductility. The uniform elongation data shown in Table. 1 was measured according to the Conside're criterion [60]:

$$\sigma \geq \left(\frac{\partial\sigma}{\partial\varepsilon}\right)_{\dot{\varepsilon}} \tag{15}$$

where σ and ε are the true stress and the true strain respectively. The 4.3 % uniform elongation of the 15 min cold weld sample is much improved in comparison with the 3.3 % of 2 h cold weld sample. To further investigate the deformation behavior of the samples, the strain hardening rate curves of the three samples were plotted in Fig. 7(b). The 2-h cold weld sample has a curve that points to the bottom left compared to the curves of the 1 h and 2 h cold weld samples. This indicates that the 2 h cold weld sample cannot be consolidated and experiences plastic instability earlier, resulting in limited uniform elongation. This observation is consistent with the uniform strain data. Typically, weak interfaces between reinforcements and the matrix in MMC act as sites of crack initiation and propagation and often do not allow load sharing between reinforcements [61–63]. It appears that the sample with a nanolaminate structure has better ductility. However, further experiments are required to confirm the positive influence of the nanolaminate structure on tensile ductility, especially considering that the mean grain size of the 2 h cold weld sample (340 nm) is significantly finer than that of the 15 min cold weld sample (480 nm).

To investigate the influence of the grain size difference on ductility, a nanolaminated Al/Al_2O_3 composite with a grain size of 320 nm was produced using the 0-h cold welding process. In this process, spherical Al powder with 1 wt% stearic acid was milled at 450 rpm and room temperature for only 1 h, resulting in Al powder flakes with a thickness of several hundred nanometers (~500 nm). The flake powders were then aligned under a pressure of 500 MPa by compaction in a column (Φ 40 × 30 mm). Sintering in a flowing Ar atmosphere at 550 °C for 2 h and subsequent hot extrusion at 500 °C with an extrusion ratio of 20:1 and a ram speed of 0.5 mm/min consolidated the flake powders.

The tensile stress-strain curves and the strain hardening rate curves are also plotted in Fig. 10. Fig. 8(a) shows that the 0 h cold weld sample (320 nm) has almost similar 0.2,σ-YS. (~ 311Mpa) and,σ-UTS. (395 MPa) compared to the 2 h cold sweat sample. However, the,-*t*. Of 12.82 % and the,-*u*. Of 6.5 % for the 0 h cold weld sample (320 nm) are significantly increased compared to the values of 6.7 % and 3.3 % for the 2 h cold weld sample. In addition, the strain hardening rate curves in Fig. 8(b) show a similar result that the 0 h cold welding sample (320 nm) with nanolaminate structure has better strain hardening ability. It can be concluded that the Al/Al_2O_3 composite with nanolaminate structure has more balanced tensile strength and ductility than the random structure with homogeneously distributed Al_2O_3 nanoplatelets and equiaxed grains.

Fig. 11(a) illustrates the stress distribution at the contact surface between the two flakes. As expected, the highest stress concentration is observed at this interface, indicating the region where sintering is most likely to occur. This high stress concentration results from the compressive forces acting during the collision between the flakes. In addition, the solid mechanics simulation provides valuable parameters for the phase field simulation equations. These parameters include: a) Maximum Stress at Contact Interface ($\Omega_{ij,\max}$): This parameter represents the peak stress experienced at the interface between the flakes. It serves as a measure of the driving force for sintering initiation. b) Stress at Flake's Center (σ_0): This parameter reflects the internal stress distribution within the flakes. It influences the sintering behavior and the evolution of the microstructure.

Fig. 11(b) demonstrates the displacement of the upper flake

Table 2
Strengthening contributions calculated using analytical model.

Cold weld sample	$\Delta\sigma_{H-P}$, MPa	$\Delta\sigma_{OR}$, MPa	$\Delta\sigma_{GND}^{CTE}$, MPa	$\Delta\sigma_{GND}^{EM}$, MPa	$\Delta\sigma_{Al_2O_3}^{dis}$, MPa	σ_{ym}, MPa	$\Delta\sigma_{Al_2O_3}^{L-T}$, MPa	R,%
15 min	115	0	75	42	86	177	78	22.67
1 h	130	48	75	42	98	187	74	19.83
2 h	141	48	75	42	98	198	74	18.68

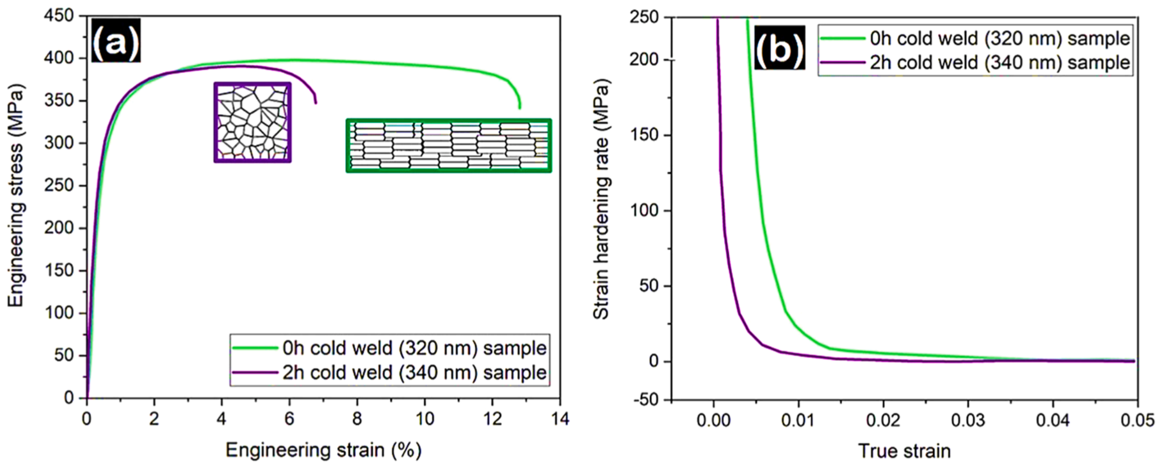

Fig. 10. (a)Tensile stress-strain curves of the 0 h cold weld (320 nm) sample and the 2 h cold weld (340 nm) sample. The schematic diagrams of the material architecture are shown next to the corresponding curves. Numbers in the brackets are the mean grain sizes. (b)Strain hardening rate curves of the 0 h cold weld (320 nm) sample and the 2 h cold weld (340 nm) sample.

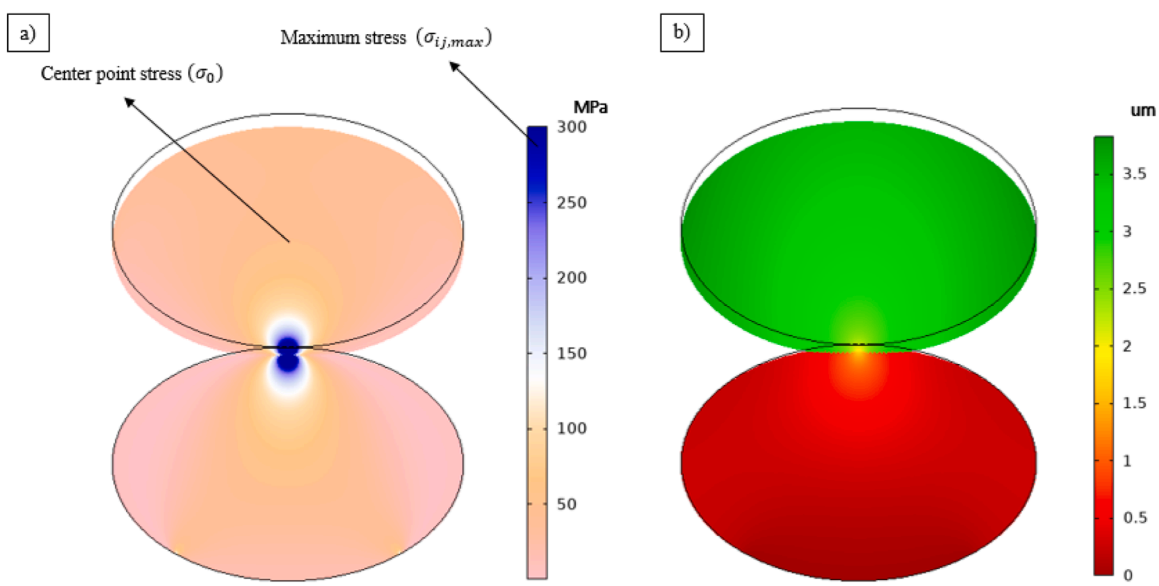

Fig. 11. The results of the simulation of solid mechanics on two flake particles in collision, (a) distribution of von Mises stresses and (b) distribution of displacement.

compared to the lower flake. The displacement of the lower flake is restricted due to the fixed boundary condition imposed upon it. This observation suggests that flakes fixed in place during the sintering process will experience reduced displacement.

The initial arrangement of the flakes, as shown in Fig. 12, represents a disordered configuration with random alignments and spacing between the individual flakes. As the simulation of Fig. 12 progressed over 1000 to 20,000 steps, the flakes exhibited a remarkable necking due to non-uniform deformation. The driving force behind necking is the reduction in surface energy, which favors the coalescence of adjacent flakes to minimize the overall energy of the system. With continued sintering, the necking process led to the formation of distinct grain boundaries between the flakes. These grain boundaries represent the interfaces at which the individual flakes merge to form a cohesive solid structure. At the same time, the porosity or void spaces, between the flakes gradually decreased, contributing to the development of a denser and more compact structure. A notable observation during the sintering process was the overall shrinkage of the flake structure. This shrinkage is attributed to the rearrangement and compaction of the flakes as they grow together and form a denser arrangement. The microstructural evolution of the flakes from an initially disordered state to a cohesive and dense structure is evidence of the transformative power of the sintering process.

Fig. 13 illustrates a finer-grained structure with increasing grain boundary formation over time. In contrast to larger flakes, finer flakes have a higher residual porosity after sintering. This is due to the larger number of triple points in finer-grained samples, where porosity tends to persist, making it more difficult to remove within the same sintering time as larger flakes. Fig. 13 shows that fine-grained samples exhibit a more pronounced polygonization after sintering, with the grains taking on a hexagonal shape due to the higher number of neighboring grains. This is in contrast to the coarse-grained samples, where a limited number of neighbors leads to fewer facets and more irregular grain shapes. Increased polygonization in fine-grained structures leads to more stable, hexagonally shaped grains that grow more slowly, which has an effect on material properties such as strength, ductility and conductivity.

Ultrafine-grained metals often exhibit less strain hardening, which is attributed to improved dynamic recovery and limited dislocation interactions [3,8,14,64-66]. However, studies [16,67-69] have found that

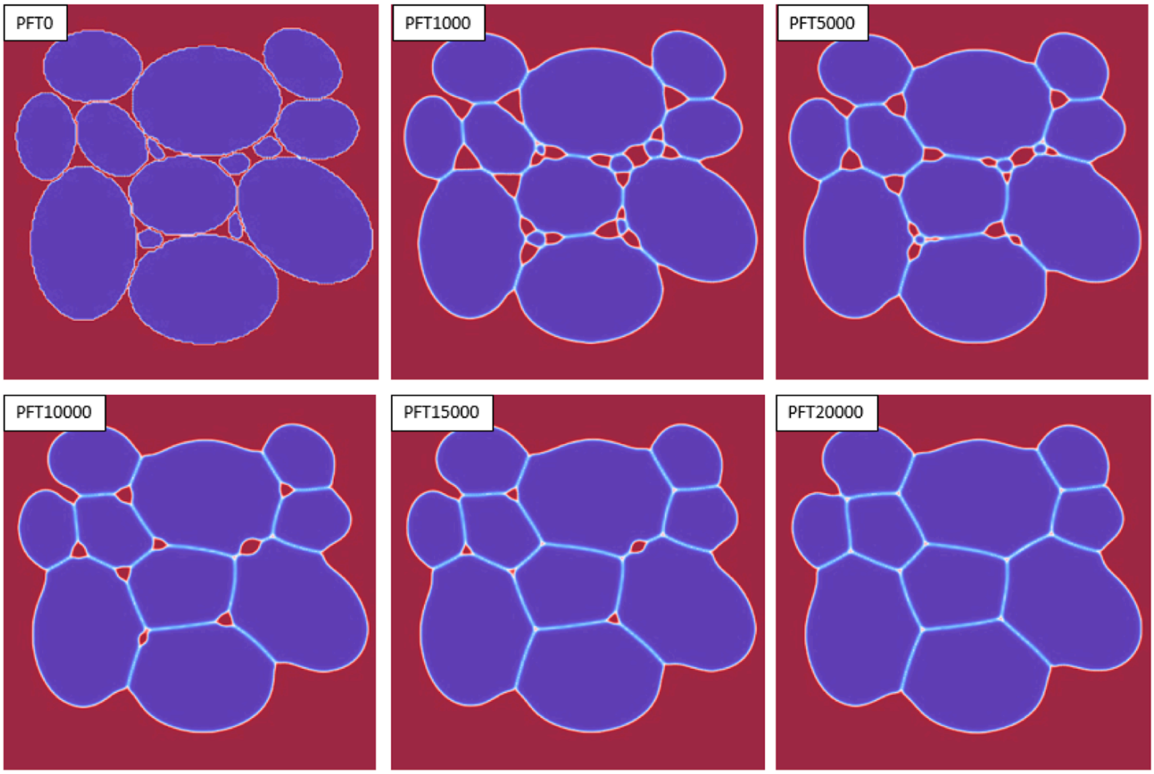

Fig. 12. The result of simulating the sintering of larger size flakes during the process over time.

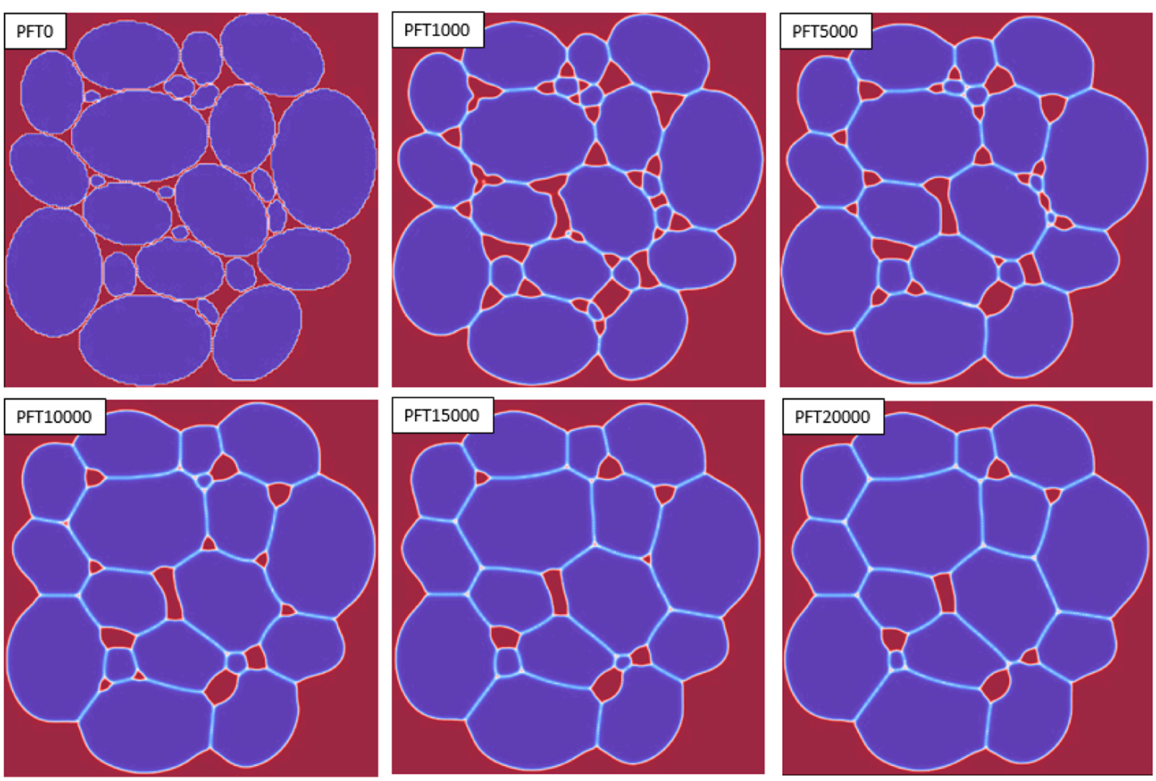

Fig. 13. The result of simulating the sintering of smaller size flakes during the process over time.

the dispersion of nanoscale Al_2O_3 particles into an Al matrix can promote the accumulation of dislocations, which improves strain hardening and elongation. In contrast to these findings, our study shows that the 2 h cold-welded Al/ Al_2O_3 nanocomposites with their larger and randomly dispersed nanoplatelets hinder dislocation movement, in contrast to the 0 h sample where finer nanoplatelets at the grain boundaries allow more dislocation activity, which is reflected in a higher dislocation density after the test (1.1×10^{14} m^{-2} to 5.6×10^{14} m^{-2}). The 1 h specimen with a semi-ordered structure also shows similar strain and strain hardening, indicating that the microstructural arrangement allows sufficient dislocation movement [3,8,14,64-66]. The 0 h specimen's resistance to defect propagation [16,67-69] is likely due to its nanolaminate architecture, which favours mechanisms such as interlayer delamination and crack deflection, which is also observed to a lesser extent in the 1 h specimen. Our results, supported by experimental and simulation data, highlight the crucial role of flaky Al particles and the cold welding process in developing the microstructure of Al/Al_2O_3 nanocomposites for improved mechanical properties, taking advantage of the strain hardening capacity and reinforcement efficiency of Al_2O_3.

5. Conclusions

The present study focused on the designability of the microstructural design of Al/Al_2O_3 nanocomposites by a combination of cold welding of flaky particles and pressure-assisted sintering and verified by experiment and discrete element method simulation. The findings are given as follows:

1. The BM process successfully converted spherical Al powders into flaky particles, which, after 3 h of milling, achieved optimal dimensions for use as building blocks in Al/ Al_2O_3 composites. The process of cold-welding during BM was instrumental in creating HAGBs and enhancing interfacial bonding by integrating Al_2O_3 particles into the Al matrix.
2. Variations in cold welding times led to distinct microstructural architectures: a laminated structure after 15 min, a lamellar particle shape after 2 h, and a mixed structure after 1 h of welding. These structures were confirmed by TEM analysis, which also showed how the distribution of Al_2O_3 nanoplatelets was affected by the welding duration, impacting the grain morphology and size.
3. Mechanical testing revealed a direct correlation between cold welding time, grain structure, and mechanical properties. Higher UTS was observed in the 2 h cold-welded specimens with lower ductility, while the 15 min cold-welded specimens showed a good balance of UTS and ductility. The distribution and orientation of Al_2O_3 platelets were crucial, with platelets within the grain interior enhancing strength via the Orowan mechanism but reducing ductility, and those on the lamellar boundaries providing a balance between strength and ductility. Grain refinement was identified as a significant contributor to the material's strength, particularly in the 15-min cold-welded samples where aligned nanoplatelets facilitated improved strain hardening and deformation behavior.
4. Simulation and experimental data consistently show that the sintering process drives the transition from disordered to ordered microstructures, with the formation of necking, the development of grain boundaries and a reduction in porosity due to densification contributing to the mechanical strength and ductility of Al/ Al_2O_3 nanocomposites.
5. Fine-grained simulations show increased porosity and polygonization and reflect the experimental evidence that the presence of finely dispersed Al_2O_3 nanoplatelets in the aluminum matrix is crucial for strain hardening and ensuring grain stability, which improves the mechanical properties of the composite.
6. The simulations confirm the experimental observations by emphasizing the importance of the stress concentration at the flake interfaces. This stress is crucial for triggering sintering-induced transformations such as necking and grain boundary formation, which are essential for optimizing the mechanical behavior of Al/ Al_2O_3 nanocomposites.

Funding

No funding was received for conducting this study.

CRediT authorship contribution statement

Behzad Sadeghi: Writing – original draft, Validation, Project administration, Investigation, Funding acquisition, Visualization, Data curation, Formal analysis, Conceptualization, Writing – review & editing. **Behzad Sadeghian:** Software, Methodology, Conceptualization, Writing – original draft. **Pasquale Cavaliere:** Project administration, Funding acquisition, Validation, Conceptualization, Data curation, Writing – review & editing. **Aboozar Taherizadeh:** Visualization, Data curation, Formal analysis, Conceptualization, Writing – review & editing.

Declaration of competing interest

The authors declare that they have no known competing financial interests or personal relationships that could have appeared to influence the work reported in this paper.

Supplementary materials

Supplementary material associated with this article can be found, in the online version, at doi:10.1016/j.mtla.2024.102083.

References

[1] Y. Karabulut, R. Ünal, Additive manufacturing of ceramic particle-reinforced aluminum-based metal matrix composites: a review, J. Mater. Sci. 57 (41) (2022) 19212–19242.
[2] B. Sadeghi, P. Cavaliere, A. Perrone, Effect of Al_2O_3, SiO2 and carbon nanotubes on the microstructural and mechanical behavior of spark plasma sintered aluminum based nanocomposites, Part. Sci. Technol. (2018) 1–8.
[3] M. Rezayat, Deformation mechanism in particulate metal matrix composites, J. Alloys Compd. 890 (2022) 161512.
[4] B. Sadeghi, B. Sadeghian, A. Taherizadeh, A. Laska, P. Cavaliere, A. Gopinathan, Effect of porosity on the thermo-mechanical behavior of friction-stir-welded spark-plasma-sintered aluminum matrix composites with bimodal micro- and nano-sized reinforcing Al_2O_3 particles, Metals (Basel) 12 (10) (2022) 1660.
[5] D. Zhang, Ultrafine grained metals and metal matrix nanocomposites fabricated by powder processing and thermomechanical powder consolidation, Prog. Mater. Sci. 119 (2021) 100796.
[6] B. Sadeghi, P. Cavaliere, C.I. Pruncu, Architecture dependent strengthening mechanisms in graphene/Al heterogeneous lamellar composites, Mater. Charact. (2022) 111913.
[7] P. Lava Kumar, A. Lombardi, G. Byczynski, S.V.S. Narayana Murty, B.S. Murty, L. Bichler, Recent advances in aluminium matrix composites reinforced with graphene-based nanomaterial: a critical review, Prog. Mater. Sci. 128 (2022) 100948.
[8] B. Sadeghi, P. Cavaliere, C.I. Pruncu, M. Balog, M. Marques de Castro, R. Chahal, Architectural design of advanced aluminum matrix composites: a review of recent developments, Crit. Rev. Solid State Mater. Sci. (2022) 1–71.
[9] H. Sun, F. Saba, G. Fan, Z. Tan, Z. Li, Micro/nano-reinforcements in bimodal-grained matrix: a heterostructure strategy for toughening particulate reinforced metal matrix composites, Scr. Mater. 217 (2022) 114774.
[10] C. Lu, M. Hsieh, Z. Huang, C. Zhang, Y. Lin, Q. Shen, F. Chen, L. Zhang, Architectural design and additive manufacturing of mechanical metamaterials: a review, Engineering 17 (2022) 44–63.
[11] T. Vogel, S. Ma, Y. Liu, Q. Guo, D. Zhang, Impact of alumina content and morphology on the mechanical properties of bulk nanolaminated Al_2O_3-Al composites, Compos. Commun. 22 (2020) 100462.
[12] Z. Zhang, Z. Li, Z. Tan, H. Zhao, G. Fan, Y. Xu, D.-b. Xiong, Z. Li, Bioinspired hierarchical Al_2O_3/Al laminated composite fabricated by flake powder metallurgy, Composites, Part A 140 (2021).
[13] L. Jiang, Z.Q. Li, G.L. Fan, D. Zhang, A flake powder metallurgy approach to Al_2O_3/Al biomimetic nanolaminated composites with enhanced ductility, Scr. Mater. 65 (5) (2011) 412–415.
[14] B. Sadeghi, P. Cavaliere, M. Balog, C.I. Pruncu, A. Shabani, Microstructure dependent dislocation density evolution in micro-macro rolled Al_2O_3/Al laminated composite, Mater. Sci. Eng.: A 830 (2022) 142317.
[15] B. Sadeghi, M. Shamanian, P. Cavaliere, F. Ashrafizadeh, M. Sanayei, J.A. Szpunar, Microstructural and mechanical behavior of bimodal reinforced Al-based composites produced by spark plasma sintering and FSP, Int. J. Adv. Manuf. Technol. 94 (9–12) (2018) 3903–3916.
[16] B. Sadeghi, M. Shamanian, F. Ashrafizadeh, P. Cavaliere, A. Rizzo, Friction stir processing of spark plasma sintered aluminum matrix composites with bimodal micro- and nano-sized reinforcing Al 2 O 3 particles, J. Manuf. Process. 32 (2018) 412–424.

[17] A. Shafiei-Zarghani, S. Kashani-Bozorg, A. Zarei-Hanzaki, Microstructures and mechanical properties of Al/Al_2O_3 surface nano-composite layer produced by friction stir processing, Mater. Sci. Eng.: A 500 (1–2) (2009) 84–91.
[18] G. Fan, Q. Liu, A. Kondo, M. Naito, K. Kushimoto, J. Kano, Z. Tan, Z. Li, Self-assembly of nanoparticles and flake powders by flake design strategy via dry particle coating, Powder Technol. 418 (2023) 118294.
[19] B. Sadeghi, G. Fan, Z. Tan, Z. Li, A. Kondo, M. Naito, Smart mechanical powder processing for producing carbon nanotube reinforced aluminum matrix composites, KONA Powder Part. J. (2022) 2022004.
[20] B. Sadeghi, A. Shabani, A. Heidarinejad, A. Laska, M. Szkodo, P. Cavaliere, A quantitative investigation of dislocation density in an Al matrix composite produced by a combination of Micro-/Macro-rolling, J. Compos. Sci. 6 (7) (2022).
[21] B. Sadeghi, Z. Tan, J. Qi, Z. Li, X. Min, Z. Yue, G. Fan, Enhanced mechanical properties of CNT/Al composite through tailoring grain interior/grain boundary affected zones, Composites Part B: Eng. 223 (2021) 109133.
[22] G. Williamson, R. Smallman III, Dislocation densities in some annealed and cold-worked metals from measurements on the X-ray debye-scherrer spectrum, Philos. Mag. 1 (1) (1956) 34–46.
[23] D. Lahiri, S.R. Bakshi, A.K. Keshri, Y. Liu, A. Agarwal, Dual strengthening mechanisms induced by carbon nanotubes in roll bonded aluminum composites, Mater. Sci. Eng.: A 523 (1–2) (2009) 263–270.
[24] B. Dzepina, D. Balint, D. Dini, A phase field model of pressure-assisted sintering, J. Eur. Ceram. Soc. 39 (2–3) (2019) 173–182.
[25] S.B. Biner, Programming Phase-Field Modeling, Programming Phase-Field Modeling, ISBN 978-3-319-41194-1, Springer International Publishing Switzerland, 2017, p. 2017.
[26] A. Kazaryan, Y. Wang, B.R. Patton, Generalized phase field approach for computer simulation of sintering: incorporation of rigid-body motion, Scr. Mater. 41 (5) (1999) 487–492.
[27] Y.U. Wang, Computer modeling and simulation of solid-state sintering: a phase field approach, Acta Mater. 54 (4) (2006) 953–961.
[28] C. Shen, Q. Chen, Y. Wen, J. Simmons, Y. Wang, Increasing length scale of quantitative phase field modeling of growth-dominant or coarsening-dominant process, Scr. Mater. 50 (7) (2004) 1023–1028.
[29] S. Razavi-Tousi, J. Szpunar, Microstructural evolution and grain subdivision mechanisms during severe plastic deformation of aluminum particles by ball milling, Philos. Mag. 95 (13) (2015) 1425–1447.
[30] P.P. Chattopadhyay, I. Manna, S. Talapatra, S.K. Pabi, A mathematical analysis of milling mechanics in a planetary ball mill, Mater. Chem. Phys. 68 (1) (2001) 85–94.
[31] M.P. Dallimore, P.G. McCormick, Dynamics of Planetary Ball Milling: a comparison of computer simulated processing parameters with CuO/Ni displacement reaction milling kinetics, Mater. Trans., JIM 37 (5) (1996) 1091–1098.
[32] H. Choi, J. Shin, D. Bae, The effect of milling conditions on microstructures and mechanical properties of Al/MWCNT composites, Composites, Part A 43 (7) (2012) 1061–1072.
[33] M. Broseghini, L. Gelisio, M. D'Incau, C.L. Azanza Ricardo, N.M. Pugno, P. Scardi, Modeling of the planetary ball-milling process: the case study of ceramic powders, J. Eur. Ceram. Soc. 36 (9) (2016) 2205–2212.
[34] H. Ghayour, M. Abdellahi, M. Bahmanpour, Optimization of the high energy ball-milling: modeling and parametric study, Powder Technol. 291 (2016) 7–13.
[35] L. Lü, M.O. Lai, S. Zhang, Modeling of the mechanical-alloying process, J. Mater. Process. Technol. 52 (2) (1995) 539–546.
[36] Y. Lin, B. Yao, Z. Zhang, Y. Li, Y. Sohn, J.M. Schoenung, E.J. Lavernia, Strain energy during mechanical milling: part I, Math. Model. Metallurg. Mater. Trans. A 43 (11) (2012) 4247–4257.
[37] R. Andrews, D. Jacques, M. Minot, T. Rantell, Fabrication of carbon multiwall nanotube/polymer composites by shear mixing, Macromol. Mater. Eng. 287 (6) (2002) 395–403.
[38] C.F. Burmeister, A. Kwade, Process engineering with planetary ball mills, Chem. Soc. Rev. 42 (18) (2013) 7660–7667.
[39] R. Xu, Z. Tan, D. Xiong, G. Fan, Q. Guo, J. Zhang, Y. Su, Z. Li, D. Zhang, Balanced strength and ductility in CNT/Al composites achieved by flake powder metallurgy via shift-speed ball milling, Composites, Part A 96 (2017) 57–66.
[40] D.L. Zhang, Processing of advanced materials using high-energy mechanical milling, Prog. Mater. Sci. 49 (3–4) (2004) 537–560.
[41] C. Suryanarayana, Mechanical alloying and milling, Prog. Mater. Sci. 46 (1) (2001) 1–184.
[42] Y. Lin, B. Yao, Z. Zhang, Y. Li, Y. Sohn, J.M. Schoenung, E.J. Lavernia, Strain Energy During Mechanical Milling: part II, Exp. Metallurg. Mater. Trans. A 43 (11) (2012) 4258–4265.
[43] H. Yang, K. Zhao, J. Nie, X. Liu, The enhanced superplasticity of a 2024 matrix nanocomposite reinforced by TiC particles, Mater. Sci. Eng.: A 774 (2020) 138926.
[44] X. Zhang, S. Li, L. Liu, D. Pan, L. Gao, X. Ji, K. Kondoh, Balanced development in strength-ductility of ultrahigh-strength aluminum matrix composites by controlled oxidation method, Mater. Sci. Eng.: A 804 (2021) 140781.
[45] G.M. Le, A. Godfrey, N. Hansen, W. Liu, G. Winther, X. Huang, Influence of grain size in the near-micrometre regime on the deformation microstructure in aluminium, Acta Mater. 61 (19) (2013) 7072–7086.
[46] O.V. Mishin, A. Godfrey, T. Yu, N. Hansen, D.J. Jensen, Evolution of microstructure and texture during recovery and recrystallization in heavily rolled aluminum, IOP Conf. Ser.: Mater. Sci. Eng. 82 (2015) 012083.
[47] M. Balog, T. Hu, P. Krizik, M.V. Castro Riglos, B.D. Saller, H. Yang, J. M. Schoenung, E.J. Lavernia, On the thermal stability of ultrafine-grained Al stabilized by in-situ amorphous Al_2O_3 network, Mater. Sci. Eng.: A 648 (2015) 61–71.
[48] M. Balog, L. Orovcik, S. Nagy, P. Krizik, M. Nosko, P. Oslanec, P. Zifcak, To what extent does friction-stir welding deteriorate the properties of powder metallurgy Al? J. Mater. Res. Technol. 9 (3) (2020) 6733–6744.
[49] P. Krizik, M. Balog, M. Nosko, M.V.C. Riglos, J. Dvorak, O. Bajana, Ultrafine-grained Al composites reinforced with in-situ Al3Ti filaments, Mater. Sci. Eng.: A 657 (2016) 6–14.
[50] M. Balog, P. Krizik, M. Nosko, Z. Hajovska, M. Victoria Castro Riglos, W. Rajner, D.-S. Liu, F. Simancik, Forged HITEMAL: al-based MMCs strengthened with nanometric thick Al 2 O 3 skeleton, Mater. Sci. Eng.: A 613 (2014) 82–90.
[51] M. Balog, F. Simancik, M. Walcher, W. Rajner, C. Poletti, Extruded Al–Al_2O_3 composites formed in situ during consolidation of ultrafine Al powders: effect of the powder surface area, Mater. Sci. Eng.: A 529 (2011) 131–137.
[52] C.Y. Barlow, N. Hansen, Y.L. Liu, Fine scale structures from deformation of aluminium containing small alumina particles, Acta Mater. 50 (1) (2002) 171–182.
[53] L. Jiang, H. Yang, J.K. Yee, X. Mo, T. Topping, E.J. Lavernia, J.M. Schoenung, Toughening of aluminum matrix nanocomposites via spatial arrays of boron carbide spherical nanoparticles, Acta Mater. 103 (2016) 128–140.
[54] D. Moszczyńska, B. Adamczyk-Cieślak, B. Osiak, R. Lipiec, M. Kulczyk, J. Mizera, Microstructure and texture development in a polycrystal and different aluminium single crystals subjected to hydrostatic extrusion, Bull. Mater. Sci. 42 (3) (2019) 110.
[55] Y. Shi, Y. Lu, Z. Ni, L. Zhao, Z. Li, D.-B. Xiong, J. Zou, Q. Guo, Correlation between microstructural architecture and mechanical behavior of single-walled carbon nanotube-aluminum composites, Metall. Mater. Trans. A 51 (2) (2020) 545–551.
[56] Z.C. Cordero, B.E. Knight, C.A. Schuh, Six decades of the Hall–Petch effect–a survey of grain-size strengthening studies on pure metals, Int. Mater. Rev. 61 (8) (2016) 495–512.
[57] J.F. Nie, B.C. Muddle, Strengthening of an Al–Cu–Sn alloy by deformation-resistant precipitate plates, Acta Mater. 56 (14) (2008) 3490–3501.
[58] S. Dong, J. Zhou, D. Hui, A quantitative understanding on the mechanical behaviors of carbon nanotube reinforced nano/ultrafine-grained composites, Int. J. Mech. Sci. 101-102 (2015) 29–37.
[59] D.B. Xiong, M. Cao, Q. Guo, Z. Tan, G. Fan, Z. Li, D. Zhang, Graphene-and-copper artificial nacre fabricated by a preform impregnation process: bioinspired strategy for strengthening-toughening of metal matrix composite, ACS Nano 9 (7) (2015) 6934–6943.
[60] E.W. Hart, A theory for flow of polycrystals, Acta Metall. 15 (9) (1967) 1545–1549.
[61] H. Choi, L. Wang, D. Cheon, W. Lee, Preparation by mechanical alloying of Al powders with single-, double-, and multi-walled carbon nanotubes for carbon/metal nanocomposites, Compos. Sci. Technol. 74 (2013) 91–98.
[62] P. Cavaliere, B. Sadeghi, A. Shabani, Carbon nanotube reinforced aluminum matrix composites produced by spark plasma sintering, J. Mater. Sci. 52 (14) (2017) 8618–8629.
[63] P. Cavaliere, F. Jahantigh, A. Shabani, B. Sadeghi, Influence of SiO2 nanoparticles on the microstructure and mechanical properties of Al matrix nanocomposites fabricated by spark plasma sintering, Composites Part B: Eng. 146 (2018) 60–68.
[64] B. Sadeghi, P. Cavaliere, M. Nosko, V. TremboŠovÁ, Š. Nagy, Hot deformation behaviour of bimodal sized Al_2O_3/Al nanocomposites fabricated by spark plasma sintering, J. Microsc. 281 (1) (2021) 28–45.
[65] J. Nie, Y. Liu, F. Wang, H. Zhou, Y. Cao, X. Liu, X. An, X. Liao, Y. Zhu, Y. Zhao, Key roles of particles in grain refinement and material strengthening for an aluminum matrix composite, Mater. Sci. Eng.: A 801 (2021) 140414.
[66] R.O. Ritchie, The conflicts between strength and toughness, Nat. Mater. 10 (11) (2011) 817.
[67] F. Khodabakhshi, H. Ghasemi Yazdabadi, A.H. Kokabi, A. Simchi, Friction stir welding of a P/M Al–Al_2O_3 nanocomposite: microstructure and mechanical properties, Mater. Sci. Eng.: A 585 (2013) 222–232.
[68] B. Sadeghi, M. Shamanian, F. Ashrafizadeh, P. Cavaliere, FSW of bimodal reinforced Al-based composites produced via spark plasma sintering, Int. J. Mater. Res. 108 (12) (2017) 1045–1054.
[69] N.K. Babu, K. Kallip, M. Leparoux, K.A. AlOgab, X. Maeder, Y.A.R. Dasilva, Influence of microstructure and strengthening mechanism of AlMg5–Al 2 O 3 nanocomposites prepared via spark plasma sintering, Mater. Des. 95 (2016) 534–544.